Title: Localized electrochemical redox reactions in yttria-stabilized zirconia single crystals

Author: Christian Rodenbücher, Kristof Szot, Dominik Wrana i in.

Citation style: Rodenbücher Christian, Szot Kristof, Wrana Dominik i in. (2020). Localized electrochemical redox reactions in yttria-stabilized zirconia single crystals. "Journal of Physics: Energy" Vol. 2, no. 3 (2020), art. no. 034008, doi 10.1088/2515-7655/ab6b39

UNIWERSYTET ŚLĄSKI
W KATOWICACH

Biblioteka
Uniwersytetu Śląskiego

Ministerstwo Nauki
i Szkolnictwa Wyższego

JPhys Energy

PAPER

Localized electrochemical redox reactions in yttria-stabilized zirconia single crystals

Christian Rodenbücher[1,4] , **Kristof Szot**[2] , **Dominik Wrana**[3] , **Benedykt R Jany**[3] , **Franciszek Krok**[3] **and Carsten Korte**[1]

1   Institute of Energy and Climate Research (IEK-14), Forschungszentrum Jülich GmbH, 52425 Jülich, Germany
2   A. Chełkowski Institute of Physics, University of Silesia, 41-500 Chorzów, Poland
3   Marian Smoluchowski Institute of Physics, Jagiellonian University, 30-348 Krakow, Poland
4   Author to whom any correspondence should be addressed.

E-mail: c.rodenbuecher@fz-juelich.de

Abstract

Herein, electroreduction in yttria-stabilized zirconia are investigated by means of Hebb-Wagner polarization experiments. By performing optical and thermal microscopy on single crystals and thin films during the application of an electric field under vacuum or oxygen-tight sealed conditions, the movement of the reduction front from the cathode to the anode, which causes a blackening of the material, is monitored. When performing electrocoloration experiments on thin film samples, the progressing reaction of the blackened region was found to be inhomogeneous and evolves as a dendrite-like finger structure. The progression of the blackening fingers follow preferentially the electric field lines and thus are influenced by distortions in the field that can be caused by metallic particles embedded in the oxide. In contrast to this, in the first stage of the reduction process no significant influence of mechanically-induced dislocations on the morphology or kinetics on the electroreduction can be found. Only after a heavy electroreduction was a localized transformation of the surface region observed. There is an evolution of highly oxygen deficient ZrO_x regions, which have a characteristic checked topography pattern at the microscale level.

1. Introduction

The emissions-free energy system of the future depends on the efficient storage of energy. Hence, the development and optimization of electrochemical energy converters have become a key task. Solid oxide fuel cells (SOFCs), employing the reaction of oxygen and hydrogen to form water, have been identified as highly reliable and cost-effective energy converters [1]. They can also be operated as solid oxide electrolysis cells (SOECs) producing hydrogen by water-splitting and thus offering a complete solution for the conversion of electrical to chemical energy and vice versa [2]. However, it has become apparent that when operating such a cell in the electrolysis mode, degradation effects can occur, which eventually limit the device's lifetime [3–5]. Hence, the investigation of the solid ion conductors that are used as SOEC electrolytes under the gradients of electrical potential is of highly relevant.

Here, we focus on electroreduction phenomena in the prototype solid electrolyte, yttria-stabilized zirconia (YSZ), which also finds widespread application in technologies such as oxygen sensors, as a thermally-stable construction material or in memristive electronics [6–10]. The high ionic conductivity of YSZ is related to the partial substitution of tetravalent Zr by trivalent Y, leading to the evolution of oxygen vacancies to balance the charge in the solid solution of yttria and zirconia [11]. Although it can accommodate a large degree of non-stoichiometry, making it a very stable material, prolonged reduction leads to a blackening effect of the originally transparent material [12–14]. In particular, when YSZ is exposed to an electric field using partially blocking electrodes in Hebb-Wagner-type geometry, the local effect of electroreduction can be readily seen as a change in the transparency related to a black reaction front moving through the material from cathode to anode [15]. This effect is well-known and has been the subject of various studies in recent decades. To understand the physical

nature of the blackening, which is crucial to develop stable SOEC devices based on YSZ, approaches employing transmission electron microscopy and x-ray photoelectron spectroscopy have been followed, indicating that in the blackened regions, Zr^{4+} is reduced to a lower valence (even metallic Zr^0 has been found) [16]. This mechanism was found to be related to the formation of zirconium suboxides (ZrO_{2-x}), leading to enhanced electronic conductivity [16–18]. While such a phase transformation might be problematic for SOEC applications where a pure ionic conductivity of the solid electrolyte is needed, the possibility of changing the material properties upon electroreduction has generated a lot of attention in the field of heterogeneous catalysis. It has been reported that the catalytic activity of a metal deposited on a solid electrolyte can be increased significantly upon electrochemical treatment, which is called the NEMCA (non-Faradaic electrochemical modification of catalytic activity) effect [19]. This effect is presumably caused by an additional electrochemical supply of reactive oxygen species via the electrolyte upon anodic polarization of the metal electrode but it is very controversially discussed in the literature [20]. Depending on the contact of the electrode and the possibility of matter exchange to the surrounding gas phase, morphologic changes can also occur at the electrode during this process, which further modify its properties. In this way, the length of the three-phase boundary formed between the electrode, solid electrolyte and surrounding gas atmosphere can be changed significantly [21]. In the case of a dense and closed PLD-fabricated Pt film in a direct contact with YSZ, the oxygen accumulating below the electrode was found to lead to the evolution of bubbles in the metal film, causing the formation of cracks and eventually a partial delamination of the film [22, 23]. Detailed studies of the bubble evolution have been conducted, revealing a characteristic sequence starting from triangular bubbles on the nanoscale that coalesce to irregularly-shaped larger bubbles over the course of time [24]. Those bubbles were found to be hollow inside, but the underside of the delaminated Pt film had oxidized to PtO_x due to the high oxygen activity at the electrode/ electrolyte interface under anodic polarization [25].

A further aspect of the ionic conductance of YSZ that must be considered is the influence of internal interfaces, such as dislocations and grain boundaries [26]. The oxygen ion transport across a grain boundary in YSZ was found to be hindered due to the presence of space charge zones related to the segregation of vacancies at the dislocation sites [27]. The question as to whether ion transport along a grain boundary in a solid electrolyte is decreased or increased compared to the bulk is complex in general and contradictory results have been published [28–30]. On YSZ crystals that were mechanically deformed to generate a high density of dislocations, a significant enhancement of the ionic conductivity was found, indicating that pipe diffusion plays an important role [31]. This finding is in agreement with oxygen isotope tracer experiments on nanocrystalline YSZ, revealing an oxygen diffusion coefficient along grain boundaries that is three times higher than in the bulk [32]. In another study using the same technique, however, the opposite effect, namely a hindered diffusion along the grain boundary, was found [33]. The reasons for this discrepancy could relate to difficulties in sample preparation, as segregation effects or the evolution of microcracks can have a significant impact on the obtained results. Regarding simulation studies using molecular dynamics, no enhancement or even a hindering of oxygen ion transport along grain boundaries at high temperatures has been calculated [34–36]. A recent investigation of single dislocations in YSZ by atomic resolution scanning transmission electron microscopy (STEM) was again in favour of easy diffusion along dislocations, proposing that the interplay of a tensile strain field and dopant segregation leads to the formation of a path with faster ionic conductivity around the core of the dislocation [37].

The impact of strain and dislocations on the ionic transport in YSZ thin films has been addressed in many studies. By depositing thin films on substrates with different lattice constants such as Y_2O_3, Lu_2O_3, or Sc_2O_3 or by fabricating YSZ/Y_2O_3 heterostructures, an increase in ionic conductivity with the lattice mismatch and with the increasing number of phase boundaries have been observed [38–40]. These findings agree with theoretical calculations, indicating a distinct correlation between the tensile strain and ion diffusion up to a critical value of the strain [41]. However, the ion transport measurements also obtained on thin film samples display a significant scattering and there are reports that conclude no or only a negligible impact of strain and dislocations [42]. The reason for these ambiguous results may be related to the impact of the film texture and grain size, making it difficult to compare thin films prepared under different conditions and to separate strain effects from grain boundary effects [43]. This illustrates that the nature of conductance in metal oxides is complex, but due to the high technological relevance for their use in energy converters, a further detailed analysis is of the utmost importance.

Here, we focus on the effect of electroreduction of YSZ to pinpoint the potential failure mechanisms of SOECs. We use single crystals as well-defined starting materials and conduct the experiments under clean high vacuum conditions. This approach has been followed in many studies on solid metal oxides to investigate electrically induced redox phenomena [44–47]. The present study is partially based on our previous investigation of electroreduction effects in $SrTiO_3$ [48]. In this material, the electroreduction leads to local self-doping inducing filamentary current paths for electronic conductivity turning the initially insulating material into an electronic conductor. This transformation was found to be strongly influenced by the presence of dislocations that act as preferential reduction sites [49]. In this article, we aim to answer the question of whether

similar effects are also present in YSZ. Although both materials share some similarities as transition metal oxides where valence change and electronic conductivity can be introduced via redox processes, the ionic conductivity of YSZ is much higher than that of $SrTiO_3$ and hence differences in the kinetics of the transformation are to be expected. In our investigation, we placed special emphasis on the role of extended defects such as dislocations, geometrical distortions or secondary phases. We analyse different states of the material degradation, starting from short electroreduction where we compare single crystals with different dislocation densities, via the investigation of YSZ thin films to make the movement of the reduction front and its morphologic evolution on the microscale visible up to heavy electroreduction, resulting in a distinct surface transformation and the evolution of new phases.

2. Methods

2.1. Electroreduction of single crystals
Commercial ZrO_2 single crystals doped with 9.5 mol% Y_2O_3 produced by skull growth (Crystec, Berlin, Germany) were used. The crystal samples, with a thickness of 0.5 mm, were aligned along the (100) direction and both sides were polished. As electrical contacts, Pt electrodes were deposited on the crystal surfaces by sputtering. The electroreduction experiments were conducted under high vacuum conditions ($<10^{-6}$ mbar) and maintained by a turbomolecular pump (Leybold, Cologne, Germany). The sample was positioned on a heater at 400 °C and an external power supply (BOP 1000 M, Kepco, Flushing, USA) was used to apply a voltage of 1 kV via a series resistor of 100 kΩ, thus providing a current compliance at 10 mA. Optical *in situ* analysis of the electrocoloration was performed by a microscope (Stemi2000, Zeiss, Oberkochen, Germany) in combination with a digital camera (Powershot, Canon, Tokyo, Japan), while thermal imaging was obtained by means of an infrared camera (X6540sc, FLIR Systems, Täby, Sweden).

2.2. Electroreduction of thin films
Thin films of YSZ were prepared by means of pulsed laser deposition (PLD) using a KrF ($\lambda = 248$ nm) excimer laser (ComPEX 201, Lambda-Physik, Göttingen, Germany). As substrates, polished sapphire substrates with a size of $10 \times 10 \times 0.5$ mm^3 in (0001) orientation (TBL Kelpin, Neuhausen, Germany) were used and as the target, polycrystalline YSZ ceramics (HTM Reetz, Berlin, Germany) was employed. After the deposition of 100 μm-thick YSZ layers on the substrates, Pt electrodes were sputtered and, finally, a thin cover layer of Al_2O_3 to partially seal the electrolyte from the ambient was applied by PLD. In this way, a Hebb-Wagner type geometry could be established with the blocking electrode negatively poled. For electrical polarization, a manual electric probe system (SÜSS MicroTec, Garching, Germany) equipped with a light microscope, a heater (750 °C) and contacts for applying an electrical voltage connected to a power supply (1 kV, Heinzinger, Rosenheim, Germany) were used. The spatial evolution of the electrocoloration front during polarization was analysed *in situ* by a CCD camera.

2.3. Analytical methods
The single crystal samples were analysed after the electroreduction at first by optical inspection. Using optical microscopy in transmission light mode, as well as in reflection mode with polarized light (Axio imager, Zeiss, Oberkochen, Germany), the morphology of the electroreduced areas was imaged. Scanning electron microscopy (SEM) imaging in terms of secondary electrons SE (topography) and backscattered electrons BSE (chemical contrast), in combination with energy-dispersive x-ray spectroscopy (EDX), was performed at 5 keV electron energy (Quanta 3D FEG, FEI, Hillsboro, USA). The EDX maps were recorded in hyperspectral mode i.e. in each spatial pixel full EDX spectrum was recorded. After the acquisition, the EDX data were bremsstrahlung background deconvoluted pixel by pixel to produce final background free net counts maps and line profiles. The surface topography was mapped by atomic force microscopy (AFM) in contact mode (Cypher S, Asylum Research, Santa Barbara, USA).

3. Results

3.1. Short electroreduction in single crystals
In order to follow the electroreduction in YSZ single crystals, we deposited two oblong Pt electrodes on the surface, which were separated by 3 mm from each other. After heating the sample under high vacuum conditions to 400 °C, the electrodes were connected to a voltage source of 1 kV with a 100 kΩ series resistor as illustrated in figure 1(a). The current recorded during electroreduction is shown in figure 1(b). It can be seen that the current increased with the degradation time almost linearly but stayed in the μA range. This indicates that within the observed time window of 80 min, the electronic conductivity related to the ongoing electroreduction
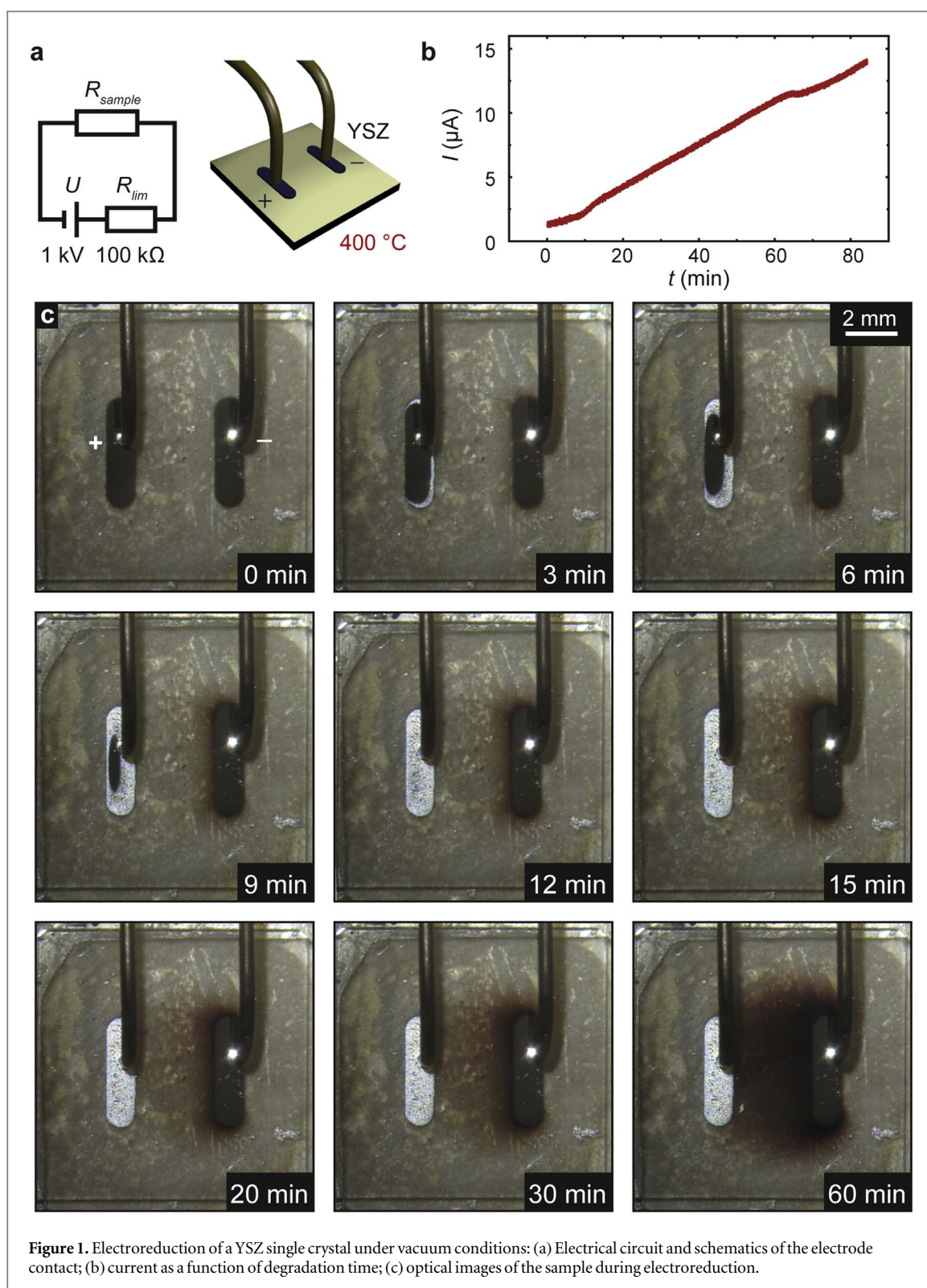
Figure 1. Electroreduction of a YSZ single crystal under vacuum conditions: (a) Electrical circuit and schematics of the electrode contact; (b) current as a function of degradation time; (c) optical images of the sample during electroreduction.

only increased slightly. However, the effect on the colour of the sample was remarkable. As is shown in the optical photographs obtained during the electroreduction process (figure 1(c)), a blackening of the crystal started directly after turning on the voltage. The electrocoloration front evolved from the cathode (right electrode in figure 1(c)) and then proceeded towards the anode over time. Simultaneously, the anode (left electrode in figure 1(a)) began to flake off gradually. This further illustrates that the current was mainly ionic and the evolving oxygen gas at the anode formed bubbles in the sputtered Pt electrode, which eventually ruptured. As the cathode consisted of sputtered Pt, which can be regarded as gas-tight, and additionally the vacuum atmosphere provided only a reduced amount of oxygen, the oxygen incorporated into the crystal is much lower than the oxygen that is transported and eventually released from the anode.
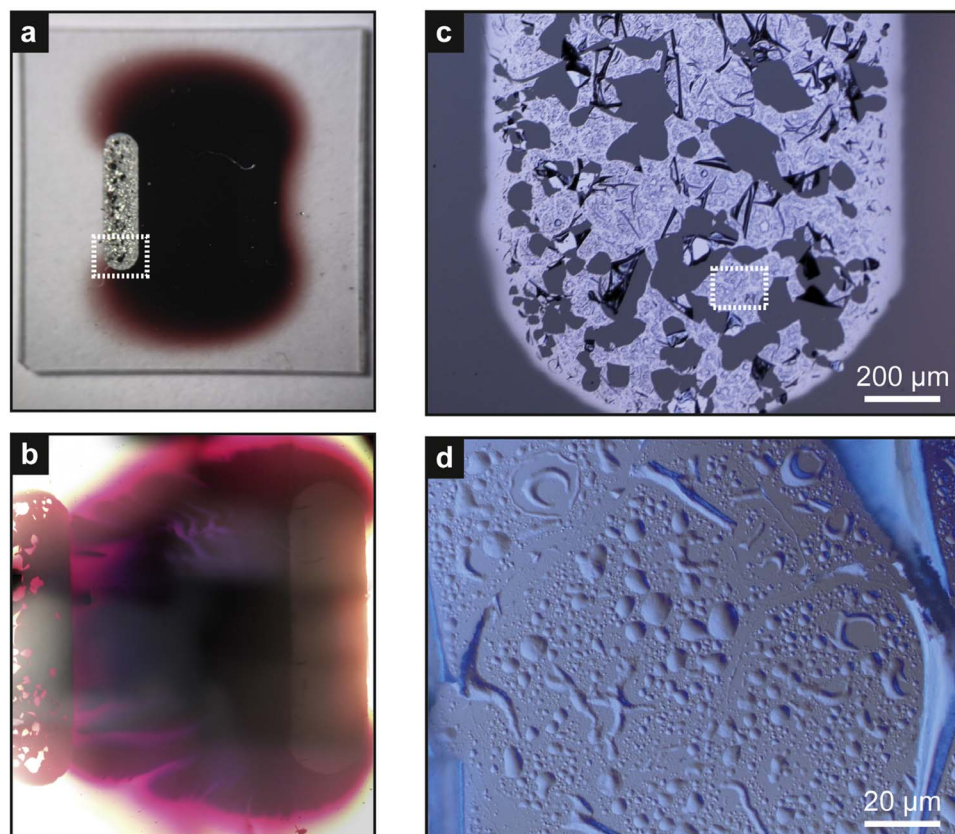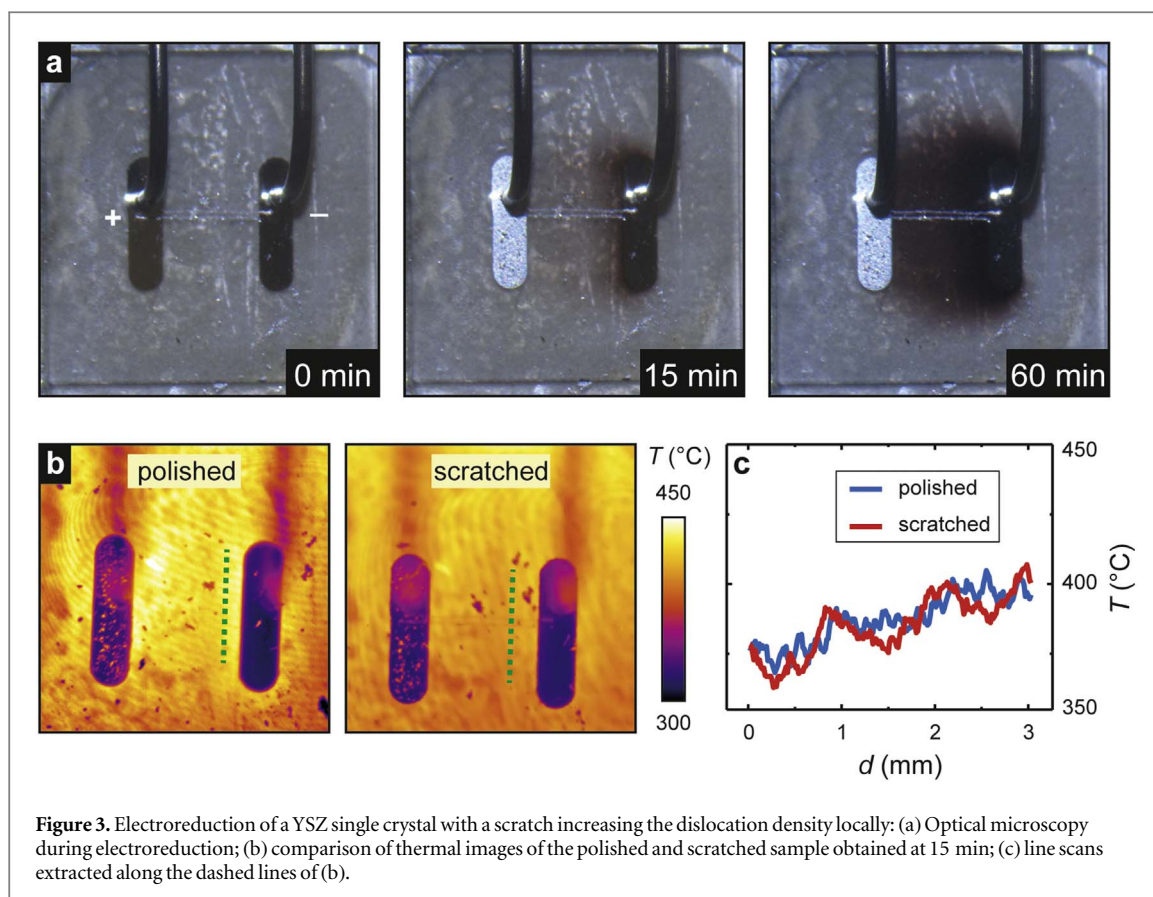
Figure 2. Analysis of the electroreduced sample by optical microscopy. (a) Overview of the crystal in reflection light mode; (b) the blackened area in transmission light mode; (c) the lower part of the anode in reflection light mode with phase contrast (dashed area in a); (d) magnification of (c).

After the electroreduction had been conducted for 80 min, the changes in the sample were investigated *ex situ* by optical microscopy. In figure 2(a), the overview of the sample in reflection light mode is shown, revealing that the entire area between the electrodes has been reduced and its colour changed to reddish black. When imaging the very same area in transmission light mode however, it can be seen that the blackened area possesses a substructure with finger-like structures having different optical transmissions (figure 2(b)). This shows that although the electroreduced area mainly follows the distribution of the electric-field lines, a certain degree of localization and inhomogeneity was present.

In figures 2(c) and (d), we analyse the anode itself using optical microscopy in reflection light mode with phase contrast. The surface of the electrode that had initially been prepared by sputtering 30 nm Pt through a shadow mask changed significantly. It can be seen that the electrode area was not completely covered anymore, but that large areas with diameters of several tens of micrometres were uncovered and the Pt film had folded up, forming agglomerations protruding from the surface. Zooming in to an area still covered by Pt (figure 2(d)), a heterogeneous distribution of bubbles can be detected on the microscale. Smaller bubbles with diameters below one micrometre, as well as larger bubbles with diameters of a few micrometres, can be observed. Moreover, some bubbles also appear to have been deflated again, showing that the excorporation of oxygen at the anode during electroreduction is a highly dynamic process. As the Pt with 30 nm thickness was directly sputtered on the surface without additional layers in between, its adhesion was relatively low and it could be easily lifted when oxygen evolved at the interface. These observations of the bubble formation upon anodic polarization are in agreement with earlier reports discussed above [22–25].

In order to check whether dislocation-rich areas influence the movement of the electroreduction front, we followed the same approach as in our previous study that investigated the electroreduction of SrTiO₃ [48] and scratched the crystal with a diamond scraper. In this way, the two electrodes were connected by a line having a large density of mechanically-induced dislocations. In figure 3, optical images at the beginning, middle, and end of the electroreduction process of this sample are exemplarily shown. The parameters of the electroreduction process such as voltage, current compliance, pressure and temperature were kept constant. When comparing the distribution of the blackened region to the sample without a scratch (figure 1), no significant changes can be

Figure 3. Electroreduction of a YSZ single crystal with a scratch increasing the dislocation density locally: (a) Optical microscopy during electroreduction; (b) comparison of thermal images of the polished and scratched sample obtained at 15 min; (c) line scans extracted along the dashed lines of (b).
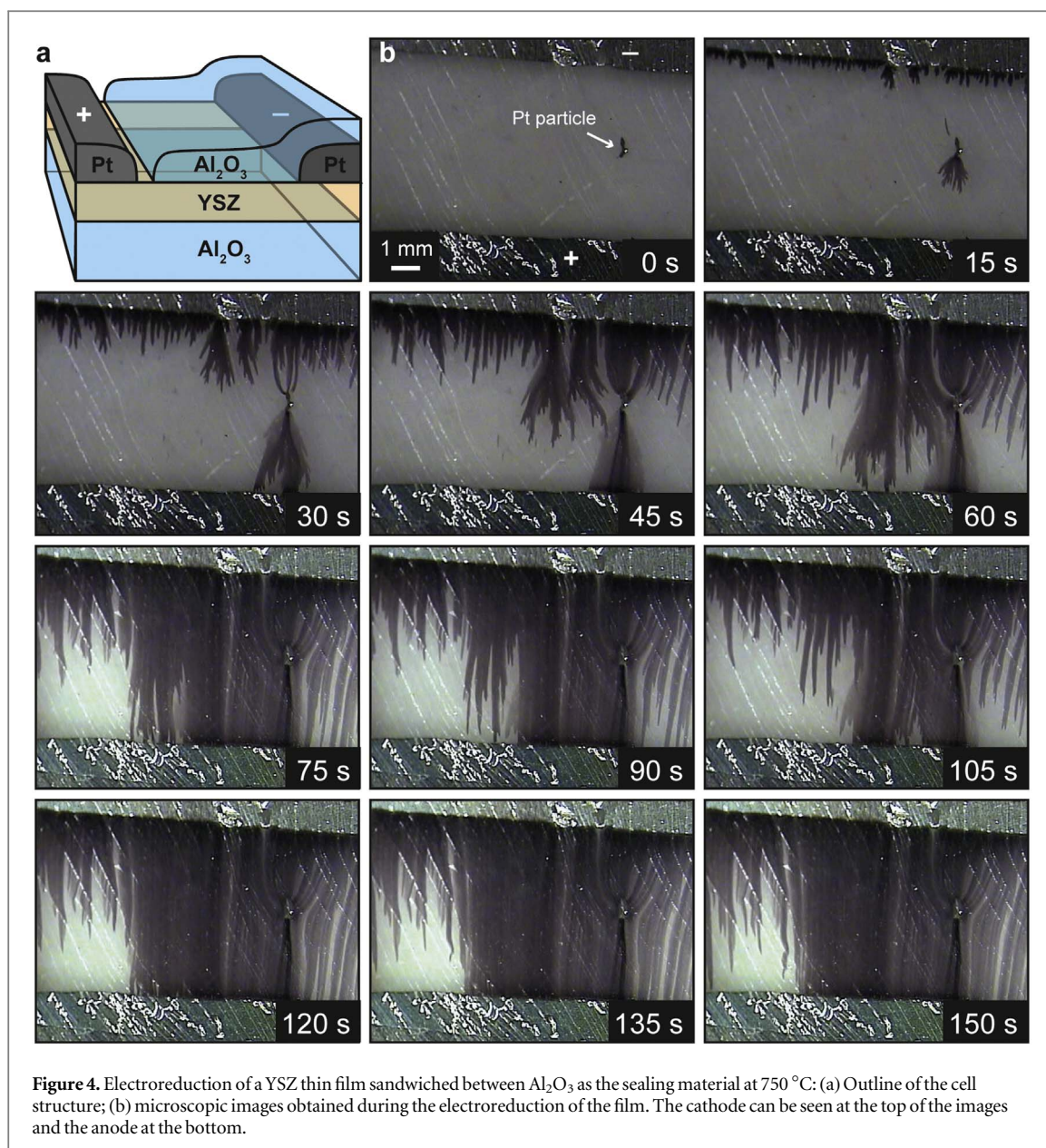
identified. The spatial distribution of the blackening as well as the electroreduction kinetics was comparable indicating that the mechanically-induced distortions did not significantly alter the degradation of the material.

To analyse the spatial distribution of electronic conductance during the electroreduction, we employed thermal microscopy and detected Joule heating effects. In figure 3(b), thermal images obtained during the electroreduction of the polished and scratched samples are compared. It can be seen that the temperature distribution in both cases is nearly identical and no increase in the temperature close to the scratch is observed. This is emphasized in the line profiles of figure 3(c), extracted along the dashed lines in between the electrodes. In general, the temperature stayed close to the base temperature of the sample during electroreduction, which shows that Joule heating effects did not prevail. As we have used the same geometry to investigate the influence of dislocations on the electroreduction of SrTiO$_3$ [48], we can also make a comparison between these two materials. While we do not observe a distinct impact of dislocations on the electroreduction of YSZ, in SrTiO$_3$ the temperature along the scratch was significantly increased, indicating a channelling of the electronic current along dislocations, acting as preferential reduction sites.
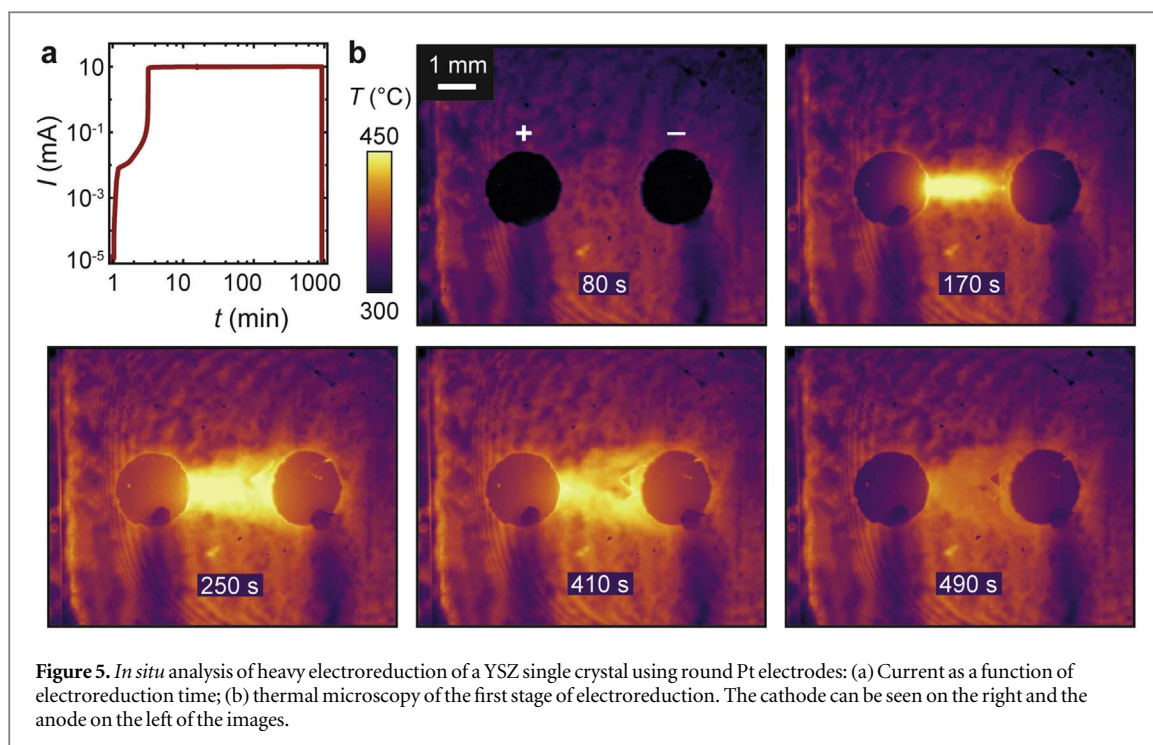
3.2. Detailed analysis of the moving reaction front

The electroreduction of single crystals using surface mounted electrodes leads to the evolution of a heterogeneous blackening area between the electrodes. For a more detailed analysis of the progressing reaction front and the evolution of the blackened region studies on thin film samples were performed. Thus, polycrystalline YSZ thin films grown on an Al$_2$O$_3$ substrate and covered with an Al$_2$O$_3$ thin film were used. The schematic of the sample structure in figure 4(a)) shows that a Hebb-Wagner polarization can be realized by sealing the surface of a thin film. Hence, similar conditions as in a vacuum electroreduction experiment of the single crystals were ascertained. As the thickness of the film (100 μm) was much lower than that of the single crystals, the moving reaction front could be easily monitored by optical microscopy. A Pt microparticle was embedded in the centre of the sample, serving as a geometrical distortion of the electrical field. The micrographs obtained during the electroreduction process at 750 °C (figure 4(b)) reveal the evolution of dendrite-like fingers. As discussed in the introduction, the reduced phase has a much better electronic conductivity compared to the unreduced one. As the ionic conductivities are comparable, the total conductivity of the reduced phase will also exceed the value for the unreduced one. In the case of the electroreduction process a better conducting phase grows into a comparable bad conducting phase. This will amplify each distortion of the reaction front as the electric field and thus the necessary ionic transport is focused to this location. The initial distortion will evolve to

Figure 4. Electroreduction of a YSZ thin film sandwiched between Al_2O_3 as the sealing material at 750 °C: (a) Outline of the cell structure; (b) microscopic images obtained during the electroreduction of the film. The cathode can be seen at the top of the images and the anode at the bottom.

the observed 'blackening fingers'. The chemical reactions related to the 'morphological instability' of reacting boundaries are thoroughly discussed in literature [15, 50, 51]. Having a closer look to the Pt microparticle, it can be observed that the first blackening fingers evolved directly at this particle as soon as the voltage (1 kV) was applied to the electrodes. This can be explained by taking into account that the metallic particle is a shortcut within the electric field and thus acts as local cathode with a high electric field gradient. Subsequently, blackening fingers also started to grow directly at the cathode (15 s). In the course of the electroreduction, some blackening fingers that started at the cathode converge towards the Pt particle, while the fingers that started at the particle diverged and reached the anode within a few seconds (30–60 s). Finally, the fingered blackening front that started at the cathode also reached the anode, leading to nearly complete electroreduced film (>75 s). The darkest blackening is reached along the initial directions of the blackening finger and in particular between the microparticle and the anode. This indicates the evolution of a channel with high electronic conductivity. This may be understood regarding the fluxes of the charge carries. Several blackening fingers connect the cathode with the microparticle which can be imagined as influent streams while only one main finger acts as effluent stream towards the anode. The presence of areas with different levels of blackening even at prolonged electroreduction of 150 s reveals that the transformation of the material can be considered as localized effect causing a substantial degree of heterogeneity.

Figure 5. *In situ* analysis of heavy electroreduction of a YSZ single crystal using round Pt electrodes: (a) Current as a function of electroreduction time; (b) thermal microscopy of the first stage of electroreduction. The cathode can be seen on the right and the anode on the left of the images.
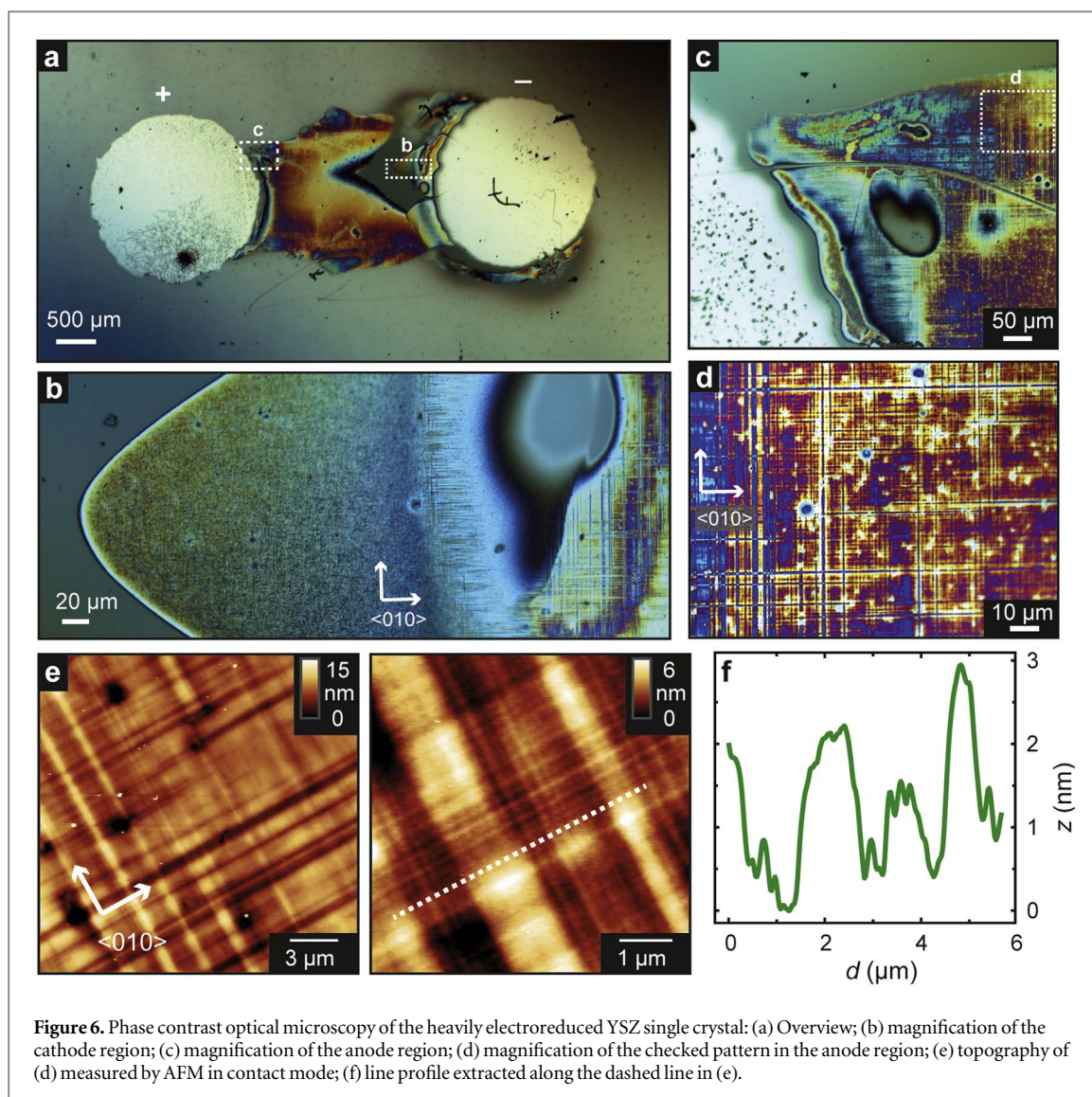
3.3. Heavy electroreduction

In the following, we concentrate on the effect of the heavy electroreduction of YSZ single crystals using the same electroreduction setup as presented in figure 1(a). Instead of using oblong electrodes, round Pt pads were deposited by sputtering to concentrate the electric field lines in the region between the electrodes. Additionally, the thickness of the Pt was increased to 100 nm in order to suppress bubble formation and electrode delamination effects. The electroreduction was again conducted at 1 kV, with 10 mA current compliance. As is illustrated in figure 5(a), the kinetics of the electroreduction were much faster than in the experiment with the oblong electrodes and the current compliance was reached within only a few minutes. Due to the higher current, the Joule heating effect was also more pronounced and a temperature increase of more than 50 °C occurred in the first stage of the electroreduction as revealed by thermal microscopy (figure 5(b)). Also, the morphology of the sample already changed in the first stage of electroreduction visible as the triangularly-shaped region in the thermal images. After the resistance of the sample decreased below the resistance of the series resistor, the voltage drop on the sample reduced to a few tens of volts, causing the temperature to decrease again. The experiment was kept running for 16 h and eventually the sample resistance decreased from originally 10^{11} Ω to below 1.8 kΩ. The change of the resistance by many orders of magnitude also indicates a change of charge carriers. Due to the electroreduction process, electronic charge carriers are induced changing the material from a pure ionic conductor into a mixed ionic-electronic conductor.

After the electroreduction, the sample was investigated by optical microscopy. Aside from the well-known electrocoloration effect causing a blackening of the region between the electrodes, the surface of this area also changed significantly, as can be seen in the image obtained using reflection light mode in combination with phase contrast (figure 6(a)). A heterogeneous region with a sharp boundary to the rest of the surface, which remained in the flat polished state, can be observed. Additionally, on the anode, a dendrite-like pattern can be seen that resembles a Lichtenberg figure [52] and presumably related to the application of a high voltage to an initially insulating sample, leading to discharge effects. The triangularly-shaped region close to the cathode, which was already visible in the thermal microscopy images, can be recognized in the (optical) micrographs. This indicates that the base of the evolving structure was already established in the first stage of heavy electroreduction. Figure 6(b) shows a magnification of this triangularly-shaped region. It becomes apparent that it has a characteristic surface structure on the microscale related to stripes aligned along the main crystallographic axes of the sample. A similar pattern can be found when zooming in on the region close to the anode (figure 6(c)). In some regions, the observed stripes form a dense checked pattern with additional irregular point-like surface distortions on the micrometre scale (figure 6(d)). To gain a detailed insight into the surface structure of the checked pattern, AFM measurements in contact mode were performed, as presented in figure 6(e). The scan area was tilted by 45° with respect to the crystallographic axes of the sample in order to avoid an interference of the motion of the AFM tip with the surface pattern. In the topography images, the checked pattern can be clearly identified. Along the dashed line on the right image in figure 6(e), a line profile was

Figure 6. Phase contrast optical microscopy of the heavily electroreduced YSZ single crystal: (a) Overview; (b) magnification of the cathode region; (c) magnification of the anode region; (d) magnification of the checked pattern in the anode region; (e) topography of (d) measured by AFM in contact mode; (f) line profile extracted along the dashed line in (e).

extracted, as shown in figure 6(f), revealing that the lines of the pattern differ by more than 2 nm in height. Taking into account that the crystal had been epipolished with a surface roughness well below 0.5 nm, we can conclude that significant material transport occurred on the surface during heavy electroreduction.

In order to characterize the chemical composition of the transformed surface region, we employed SEM with EDX. For these measurements, we employed a second sample that was also heavily electroreduced, using the same parameters as previously. In figure 7(a), the optical image of the surface close to the cathode region is shown. Although the outer shape of the transformed region is slightly different from that shown in figure 6, the inner structure with lines oriented along the crystal axis is similar, showing that the effect of surface modification by electroreduction is reproducible. In the corresponding SEM micrograph in figure 7(b) using the back-scattered electron (BSE) detector, the transformed region can clearly be identified. It appears brighter in the micrograph indicating a different chemical composition (higher average electron density, more heavy elements, i.e. oxygen deficient). We recorded an EDX spectrum in the dashed area 1 marked in figure 7(b) and compared it to a YSZ reference (pristine sample) spectrum obtained at one edge on the same crystal far from the transformed region. In order to avoid charging effects, the sample was coated with a carbon layer for the SEM investigation beforehand. Hence, the EDX spectra shown in figure 7(c) were normalized to the C K_α peak intensity. It can be seen that the peaks of Zr and Y are almost identical, while the O signal of the transformed region is significantly reduced as compared to the reference. To quantify the degree of reduction, the ratios of the measured atomic percentages of Zr and O were calculated. While in the reference region, a Zr/O ratio of 1.8 was obtained, the value in area 1 was only 1.1. This is significantly lower compared to reference region. Considering the Y_2O_3 doping this implies almost identical amount of Zr and O in the surface layer and could indicate the presence of phases with a composition close to ZrO. In figure 7(d), a magnification of the transformed region is shown. The oriented stripes that were already found by optical microscopy and AFM in figure 6 can be retrieved in the BSE
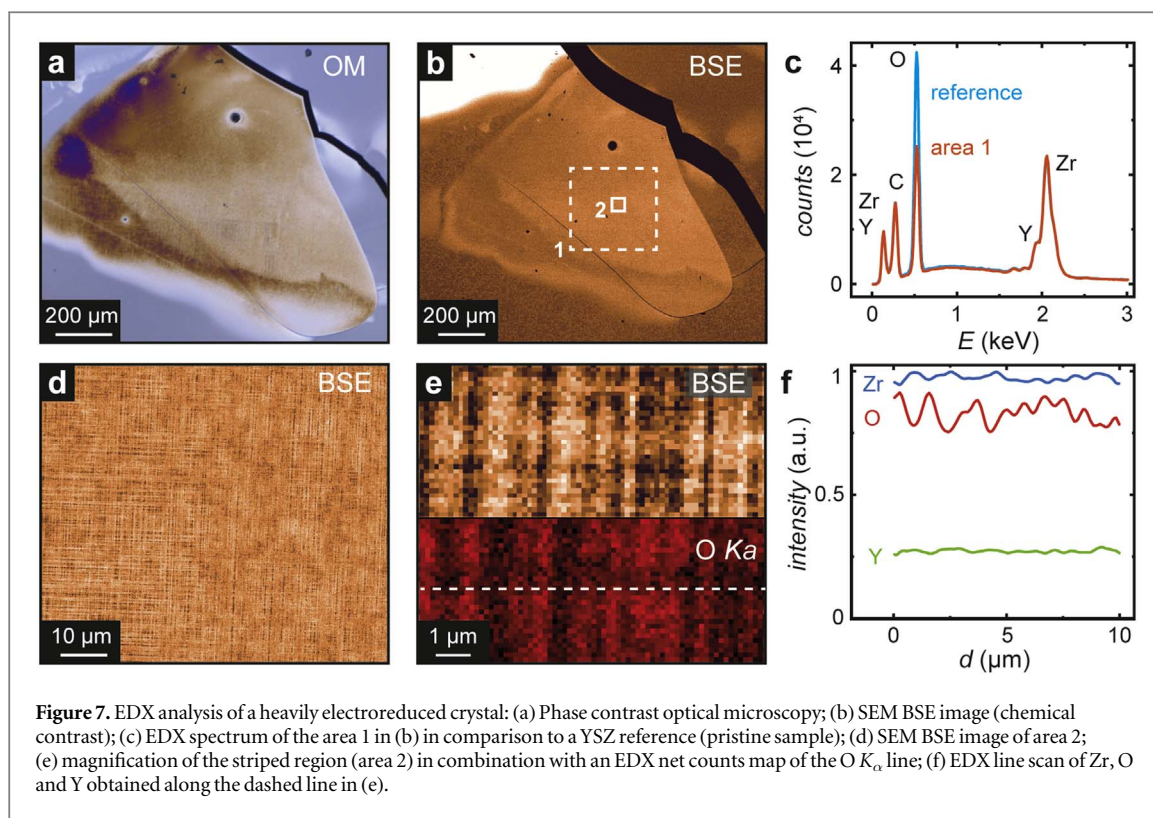
Figure 7. EDX analysis of a heavily electroreduced crystal: (a) Phase contrast optical microscopy; (b) SEM BSE image (chemical contrast); (c) EDX spectrum of the area 1 in (b) in comparison to a YSZ reference (pristine sample); (d) SEM BSE image of area 2; (e) magnification of the striped region (area 2) in combination with an EDX net counts map of the O K_α line; (f) EDX line scan of Zr, O and Y obtained along the dashed line in (e).

image. In order to elucidate the chemical composition of the stripes, EDX mapping with high magnification was obtained and is shown in figure 7(e) for the O K_α line and illustrated as a line scan in figure 7(f). It can be seen that the stoichiometry is not constant, but correlated with the topography of the stripes. By tilting the crystal and comparing the secondary electrons (SE) contrast with the backscattered electrons (BSE) contrast, we were able to conclude that the highly oxygen-deficient stripes correspond to a topographic depression and vice versa. These results could indicate that the formation of different substoichiometric ZrO_x phases on the microscale is creating a characteristic striped/checked surface pattern. The orientation of the stripes along of the main crystal axes of the original crystal suggests that the oxygen deficient region is strongly related to the surrounding, still oxygen-rich, YSZ crystal and that new dislocations have been formed compensating the lattice mismatch.

Just to estimate an electromotive force (EMF) which should be sufficient to drive a reduction process if exceeded, one could consider the free enthalpy of the formation reaction of ZrO from zirconium and oxygen. At 500 °C this would yield and equilibrium oxygen activity of 10^{-64}, respectively an EMF of 2.4 V [15, 53]. This is the thermodynamic limit. Due to the low conductivity of YSZ at this temperature, a potential difference in this order of magnitude would only allow very small current and thus only an as well very slowly proceeding reduction process. According to Levy [13], a significant increase of the electronic conductivity can be observed if the oxygen deficiency δ of $Zr_{1-y}Y_{2y}O_{2+y-x-\delta}$ is higher than 0.01. This indicates that in principle under such an oxygen activity the degradation process already sets in which will eventually lead to the formation of a new phase. However, the kinetics of the reduction process will depend significantly on the temperature (conductivity), the voltage applied (driving force) and the surrounding atmosphere (simultaneous re-oxidation), which makes it difficult to give a precise value for SOEC application, leading to significant effect within a chosen time scale.

4. Conclusions

In this work, we illustrated localized phenomena related to electroreduction in YSZ single crystals. In the first state of electroreduction, an electrocoloration (blackening) effect occurs, changing the optical properties of the crystal from its initial transparent state to opaque. This effect appears as a reaction front starting at the cathode and moving gradually to the anode. While a distinct influence of mechanically-induced dislocation on the kinetics and morphology of the blackening could not be identified, the blackened area itself exhibits an irregular structure related to the presence of 'blackening fingers'. Comparable experiments on YSZ revealed that the blackening fingers mainly follow the electric field lines and are thus influenced by distortions of the field distribution as can be caused by metallic microparticles acting as electric dipoles. Finally, after heavy reduction, not only does the colour of the crystal, but also the surface structure, change significantly, causing the local

evolution of regions exhibiting a checked pattern aligned along the crystal axes with a high amount of oxygen non-stoichiometry. Our experiments indicate that the application of electric field gradients on a solid electrolyte such as YSZ can lead to localized electroreduction, resulting in the evolution of electronically conducting paths, which could be a challenge for using the material as an SOEC electrolyte. This will be of particular importance for miniaturized SOECs with electrolyte thickness in the micrometre range where comparable electric field gradients, as in our model systems, are present. Intrinsic structural defects such as dislocations or grain boundaries do not appear to play a dominant role in this process. However, during fabrication of the electrolyte, great care should be taken to avoid the inclusion of metallic particles, as they could significantly alter the local distribution of the electric field in the electrolyte. Hence, they could act as seeds for the evolution of electroreduced current paths and thus significantly accelerate the kinetics of device degradation.

Acknowledgments

ORCID iDs

Christian Rodenbücher ⓘ https://orcid.org/0000-0001-8029-3066
Kristof Szot ⓘ https://orcid.org/0000-0001-8773-2754
Dominik Wrana ⓘ https://orcid.org/0000-0002-8239-0043
Benedykt R Jany ⓘ https://orcid.org/0000-0002-3196-7244
Franciszek Krok ⓘ https://orcid.org/0000-0002-6931-3545
Carsten Korte ⓘ https://orcid.org/0000-0001-6574-6223

References

[1] Blum L, de Haart L G J, Malzbender J, Margaritis N and Menzler N H 2016 Anode-supported solid oxide fuel cell achieves 70 000 h of continuous operation *Energy Technol.* **4** 939–42

[2] Liu M, Lynch M E, Blinn K, Alamgir F M and Choi Y 2011 Rational SOFC material design: new advances and tools *Mater. Today* **14** 534–46

[3] Frey C E, Fang Q, Sebold D, Blum L and Menzler N H 2018 A detailed post mortem analysis of solid oxide electrolyzer cells after long-term stack operation *J. Electrochem. Soc.* **165** F357–64

[4] Nechache A, Boukamp B A, Cassir M and Ringuedé A 2019 Accelerated degradation of yttria stabilized zirconia electrolyte during high-temperature water electrolysis *J. Solid State Electrochem.* **23** 871–81

[5] Mogensen M, Jensen K V, Jørgensen M J and Primdahl S 2002 Progress in understanding SOFC electrodes *Solid State Ion.* **150** 123–9

[6] Arndt B *et al* 2017 Spectroscopic indications of tunnel barrier charging as the switching mechanism in memristive devices *Adv. Funct. Mater.* **27** 1702282

[7] Liu Y, Parisi J, Sun X and Lei Y 2014 Solid-state gas sensors for high temperature applications—a review *J Mater Chem* A **2** 9919–43

[8] Di Girolamo G, Marra F, Blasi C, Serra E and Valente T 2011 Microstructure, mechanical properties and thermal shock resistance of plasma sprayed nanostructured zirconia coatings *Ceram. Int.* **37** 2711–7

[9] Kärkkänen I *et al* 2015 Impedance spectroscopy study of the unipolar and bipolar resistive switching states of atomic layer deposited polycrystalline ZrO_2 thin films *Phys. Status Solidi* a **212** 751–66

[10] Vendrell X and West A R 2018 Electrical properties of yttria-stabilized zirconia, YSZ single crystal: local AC and long range DC conduction *J. Electrochem. Soc.* **165** F966–75

[11] Kirchheim R 2018 On the mixed ionic and electronic conductivity in polarized yttria stabilized zirconia *Solid State Ion.* **320** 239–58

[12] Farley J M, Thorp J S, Ross J S and Saunders G A 1972 Effect of current-blackening on the elastic constants of yttria-stabilised zirconia *J. Mater. Sci.* **7** 475–6

[13] Levy M 1988 Model for the electrical conductivity of reduced stabilized zirconia *J. Electrochem. Soc.* **135** 1584

[14] Zhu L, Zhang L and Virkar A V 2016 Electroreduction of zirconia using embedded electrodes *J. Electrochem. Soc.* **163** F714–8

[15] Janek J and Korte C 1999 Electrochemical blackening of yttria-stabilized zirconia - morphological instability of the moving reaction front *Solid State Ion.* **116** 181–95

[16] Luerßen B, Janek J, Günther S, Kiskinova M and Imbihl R 2002 Microspectroscopy at a moving reduction front in zirconia solid electrolyte *Phys. Chem. Chem. Phys.* **4** 2673–9

[17] Siegel D A, El Gabaly F, McCarty K F and Bartelt N C 2015 *In situ* characterization of the formation of a mixed conducting phase on the surface of yttria-stabilized zirconia near Pt electrodes *Phys. Rev. B—Condens. Matter Mater. Phys.* **92** 125421

[18] Moghadam F K, Yamashita T and Stevenson D A 1983 Characterization of the current-blackening phenomena in scandia stabilized zirconia using transmission electron microscopy *J. Mater. Sci.* **18** 2255–9

[19] Vernoux P, Gaillard F, Bultel L, Siebert E and Primet M 2002 Electrochemical promotion of propane and propene oxidation on Pt/YSZ *J. Catal.* **208** 412–21

[20] Vayenas C G, Bebelis S and Neophytides S 1988 Non-Faradaic electrochemical modification of catalytic activity *J. Phys. Chem.* **92** 5083–5

[21] Opitz A K, Lutz A, Kubicek M, Kubel F, Hutter H and Fleig J 2011 Investigation of the oxygen exchange mechanism on Pt|yttria stabilized zirconia at intermediate temperatures: surface path versus bulk path *Electrochim. Acta* **56** 9727–40

[22] Mutoro E, Günther S, Luerßen B, Valov I and Janek J 2008 Electrode activation and degradation: morphology changes of platinum electrodes on YSZ during electrochemical polarisation *Solid State Ion.* **179** 1835–48

[23] Beck G and Bachmann C 2014 Oxygen removal at grain boundaries in platinum films on YSZ *Solid State Ion.* **262** 508–11

[24] Pöpke H, Mutoro E, Luerßen B and Janek J 2011 The potential of *in situ*-scanning electron microscopy—Morphology changes of electrically polarized thin film Pt(O₂)/YSZ model electrodes *Solid State Ion.* **189** 56–62

[25] Keller T F, Volkov S, Navickas E, Kulkarni S, Vonk V, Fleig J and Stierle A 2019 Nano-scale oxide formation inside electrochemically-formed Pt blisters at a solid electrolyte interface *Solid State Ion.* **330** 17–23

[26] Gregori G, Merkle R and Maier J 2017 Ion conduction and redistribution at grain boundaries in oxide systems *Prog. Mater. Sci.* **89** 252–305

[27] Guo X and Zhang Z 2003 Grain size dependent grain boundary defect structure: case of doped zirconia *Acta Mater.* **51** 2539–47

[28] Skinner S J 2019 Recent advances in the understanding of the evolution of surfaces and interfaces in solid oxide cells *Adv. Mater. Interfaces* **6** 1900580

[29] Szot K, Rodenbücher C, Bihlmayer G, Speier W, Ishikawa R, Shibata N and Ikuhara Y 2018 Influence of dislocations in transition metal oxides on selected physical and chemical properties *Crystals* **8** 241

[30] Guo X, Vasco E, Mi S, Szot K, Wachsman E and Waser R 2005 Ionic conduction in zirconia films of nanometer thickness *Acta Mater.* **53** 5161–6

[31] Otsuka K, Kuwabara A, Nakamura A, Yamamoto T, Matsunaga K and Ikuhara Y 2003 Dislocation-enhanced ionic conductivity of yttria-stabilized zirconia *Appl. Phys. Lett.* **82** 877–9

[32] Knöner G, Reimann K, Röwer R, Södervall U and Schaefer H-E 2003 Enhanced oxygen diffusivity in interfaces of nanocrystalline ZrO₂·Y₂O₃ *Proc. Natl Acad. Sci.* **100** 3870–3

[33] De Souza R A, Pietrowski M J, Anselmi-Tamburini U, Kim S, Munir Z A and Martin M 2008 Oxygen diffusion in nanocrystalline yttria-stabilized zirconia: the effect of grain boundaries *Phys. Chem. Chem. Phys.* **10** 2067

[34] Huang H C, Su P-C, Kwak S K, Pornprasertsuk R and Yoon Y-J 2014 Molecular dynamics simulation of oxygen ion diffusion in yttria stabilized zirconia single crystals and bicrystals *Fuel Cells* **14** 574–80

[35] Fisher C A J and Matsubara H 1999 Molecular dynamics investigations of grain boundary phenomena in cubic zirconia *Comput. Mater. Sci.* **14** 177–84

[36] González-Romero R L, Meléndez J J, Gómez-García D, Cumbrera F L and Domínguez-Rodríguez A 2012 A Molecular dynamics study of grain boundaries in YSZ: structure, energetics and diffusion of oxygen *Solid State Ion.* **219** 1–10

[37] Feng B, Ishikawa R, Kumamoto A, Shibata N and Ikuhara Y 2019 Atomic scale origin of enhanced ionic conductivity at crystal defects *Nano Lett.* **19** 2162–8

[38] Schichtel N, Korte C, Hesse D and Janek J 2009 Elastic strain at interfaces and its influence on ionic conductivity in nanoscaled solid electrolyte thin films—theoretical considerations and experimental studies *Phys. Chem. Chem. Phys.* **11** 3043

[39] Korte C, Peters A, Janek J, Hesse D and Zakharov N 2008 Ionic conductivity and activation energy for oxygen ion transport in superlattices—the semicoherent multilayer system YSZ (ZrO₂ + 9.5 mol% Y₂O₃)/Y₂O₃ *Phys. Chem. Chem. Phys.* **10** 4623

[40] Korte C, Keppner J, Peters A, Schichtel N, Aydin H and Janek J 2014 Coherency strain and its effect on ionic conductivity and diffusion in solid electrolytes—an improved model for nanocrystalline thin films and a review of experimental data *Phys. Chem. Chem. Phys.* **16** 24575–91

[41] Kushima A and Yildiz B 2010 Oxygen ion diffusivity in strained yttria stabilized zirconia: where is the fastest strain? *J. Mater. Chem.* **20** 4809

[42] Harrington G F, Cavallaro A, McComb D W, Skinner S J and Kilner J A 2017 The effects of lattice strain, dislocations, and microstructure on the transport properties of YSZ films *Phys. Chem. Chem. Phys.* **19** 14319–36

[43] Keppner J, Schubert J, Ziegner M, Mogwitz B, Janek J and Korte C 2018 Influence of texture and grain misorientation on the ionic conduction in multilayered solid electrolytes—interface strain effects in competition with blocking grain boundaries *Phys. Chem. Chem. Phys.* **20** 9269–80

[44] Waser R, Baiatu T and Hardtl K-H 1990 dc electrical degradation of perovskite-type titanates: II. Single crystals *J. Am. Ceram. Soc.* **73** 1654–62

[45] Long D, Creange N, Moballegh A and Dickey E C 2019 Electromigration-induced leakage current enhancement and its anisotropy in single crystal TiO₂ *J. Appl. Phys.* **125** 184101

[46] Rodenbücher C *et al* 2018 Electrically controlled transformation of memristive titanates into mesoporous titanium oxides via incongruent sublimation *Sci Rep.* **8** 3774

[47] Wang J-J, Huang H-B, Bayer T J M, Moballegh A, Cao Y, Klein A, Dickey E C, Irving D L, Randall C A and Chen L-Q 2016 Defect chemistry and resistance degradation in Fe-doped SrTiO₃ single crystal *Acta Mater.* **108** 229–40

[48] Rodenbücher C, Menzel S, Wrana D, Gensch T, Korte C, Krok F and Szot K 2019 Current channeling along extended defects during electroreduction of SrTiO₃ *Sci. Rep.* **9** 2502

[49] Marrocchelli D, Sun L and Yildiz B 2015 Dislocations in SrTiO₃: easy to reduce but not so fast for oxygen transport *J. Am. Chem. Soc.* **137** 4735–48

[50] Martin M 1994 Interface stability during reactions *Mater. Sci. Forum* **155–156** 429–44

[51] Martin M, Tigelmann P, Schimschal-Thölke S and Schulz G 1995 Solid state reactions and morphology *Solid State Ion.* **75** 219–28

[52] Merrill F H and Von Hippel A 1939 The atomphysical interpretation of lichtenberg figures and their application to the study of gas discharge phenomena *J. Appl. Phys.* **10** 873–87

[53] Kubaschewski O, Alcock C B and Spencer P J 1993 *Materials Thermochemistry* (Oxford: Pergamon)